Residual stresses in surface induction hardening of steels: Comparison between experiment and simulation

Dominique Coupard [a,*], Thierry Palin-luc [a], Philippe Bristiel [b], Vincent Ji [c], Christian Dumas [d]

[a] *ENSAM, Université Bordeaux I, Laboratoire Matériaux Endommagement Fiabilité et Ingénierie des Procédés (LAMEFIP), EA2727, Esplanade des Arts et Métiers, 33405 Talence Cedex, France*
[b] *PRISMECA, 191 Avenue. du Général Leclerc, 78220 Viroflay, France*
[c] *ENSAM, LIM (UMR CNRS 8006), 151, Bd de l'Hôpital, 75013 Paris, France*
[d] *RENAULT, Technocentre, DIMAT, TCR LAB 035, 1 Avenue du Golf, 78288 Guyancourt Cedex, France*

Abstract

Deep induction hardening has been performed on two batches of smooth cylindrical specimens with a hardening depth respectively around 2 mm and 3 mm. The distributions of axial and circumferential residual stresses are analysed for the two specimen batches by X-ray diffraction technique. The radial normal stress field is estimated through the use of the well known Moore and Evans correction. Finally, the experimental residual stresses are compared with those obtained from a multiphysic finite element modelling of the whole induction treatment process, including electromagnetic, thermal, metallurgical and mechanical phenomena. The simulated residual stress field is in good agreement with X-ray analysis especially at depths lower than one-tenth the specimen diameter. At deeper depths, a correction of the experimental X-ray analysis has been done to obtain realistic values.

Keywords: Induction hardening; X-ray diffraction analysis; FEM; Modelling

1. Introduction

The current tendency in the field of critical automotive components is to increase the performance while reducing material and processing costs such as machining, forging or hardening treatments. The current guideline is rather to use carbon steels for which fatigue performance has to be increased by an optimised surface hardening. This can be achieved by thermo-chemical or thermal treatments such as carburizing, nitriding or induction hardening.

Induction surface hardening of low alloy carbon steel is increasingly used for high stressed components, especially in the automotive industry. The process is known to offer some advantages with respect to other surface treatments such as carburizing, shot-peening, burnishing or rolling. One of the main features of induction surface treatment is the high fatigue strength improvement [1]. It is also viewed as a cleaner process than carburizing because it uses less toxic products than those used in carburizing or nitriding. Induction treatment can also be integrated into a production line because surface hardening is achieved in a few seconds.

Induction hardening gives rise in the work piece to a tough core with tensile residual stresses and a hard surface layer with compressive stresses [2]. This configuration has proved to be very effective in extending the fatigue life, i.e. delaying fatigue crack initiation [3,4]. However, the effectiveness of residual stresses is quite dependent on their distribution into the component and on their relaxation during in service fatigue loading. The distribution is affected by the component geometry, the material behaviour and the induction treatment parameters [5,6]. For example, Breen et al. [7] suspected that a large hardening depth generate less compressive residual stresses in the hardened layer than a thin one. Their evolution under cyclic loading depends on the local plastic strains experienced during fatigue [5,8]. Depending on both the residual stress field and the applied

* Corresponding author. Tel.: +33 556845347.
E-mail address: dominique.coupard@lamef.bordeaux.ensam.fr (D. Coupard).

Nomenclature

Electromagnetic modelling

a	initial slope of the B(H) curve
C	curvature of B(T)
$\vec{E}$	electric field ($V\,m^{-1}$)
$\vec{H}$	magnetic field ($A\,m^{-1}$)
$\vec{B}$	magnetic induction (T)
$\vec{J}$	electric current density ($A\,m^{-2}$)
J_s	saturated magnetisation at 0 °C
T_c	Curie temperature
μ_0	vacuum magnetic permeability ($4\pi \times 10^{-7}\,H\,m^{-1}$)
μ_r	relative magnetic permeability ($H\,m^{-1}$)
ρ_e	electric resistivity ($\Omega\,m$)
χ	electric conductivity ($S\,m^{-1}$)

Thermal modelling

C_p	material specific heat at constant pressure ($J\,kg^{-1}\,K^{-1}$)
E_b	transition energy ($J\,m^{-3}$) for the ferrite to austenite transition
h	convection coefficient ($W\,m^{-2}\,°C^{-1}$)
h_1, h_2, h_3, T_2, T_3, τ_2, τ_3	constants
$\vec{n}$	unit normal vector
s_0	standard deviation (in temperature) of the Gaussian part of equation (I.13)
T	temperature (K)
T_0	constant (°C)
T_1	constant (°C)
T_b	ferrite to austenite temperature transition (°C)
T_e	fluid temperature (°C)
T_s	surface temperature of the workpiece (°C)
$\dot{q}$	power density released or taken during phase transformations ($W\,m^{-3}$)
Q	power density wasted by joule effect ($W\,m^{-3}$)
V_0	ρCp value for $T = 0\,°C$
V_∞	ρCp value for $T \to +\infty$
λ	thermal conductivity ($W\,m^{-1}\,K^{-1}$)
λ_0	λ value for $T = 0\,°C$
λ_∞	λ value for $T \to +\infty$
ρ	mass density ($kg\,m^{-3}$)
φ_c	heat flux lost by convection ($W\,m^{-2}$)

Metallurgical modelling

$b(T)$, $c(T)$, d	material parameters
M_s	Martensitic transformation starting point in a phase transformation diagram
y	volume fraction of the new transformed phase
y_a	austenite volume fraction available for the martensitic transformation, i.e. at M_s
y_i	volume fraction of the phase i
$y_m(T)$	maximum volume fraction of the new transformed phase
t_1	time since the beginning of the phase transformation
$\tau(T)$	incubation time
z	constant
α_b	austenitisation parameter

Mechanical modelling

E	Young modulus
S_{ij}	deviatoric stress tensor
δ_{ij}	Kronecker symbol
ε^e_{ij}	elastic strain tensor
ε^p_{ij}	plastic strain tensor
ε^{th}_{ij}	thermal strain tensor $\varepsilon^{th}_{ij} = \delta_{ij} \int_{T_0}^{T} \alpha(T) dT$
ε^{tr}_{ij}	transformation strain tensor
ν	Poisson ratio
σ_0	flow stress
$\sigma_{eq,VM}$	Von-Mises equivalent stress (σ_{eq}, VM $= \sqrt{\frac{3}{2} S_{ij} S_{ij}}$)
σ_{ij}	stress tensor
ν	Poisson ratio

external fatigue loading, cracks can either initiate in the vicinity of the surface or beneath the hardened layer [9]. Therefore, it is important to determine the residual stress field in a design department to optimise the treatment for a given component. The high importance of residual stresses on the fatigue strength of materials and structures is well known [10]. Residual stresses (after cyclic relaxation if any) are considered as mean stresses superimposed with the cyclic stresses due to the fatigue loading [11]. The usual way to consider residual stresses in fatigue strength calculation is to use a multiaxial fatigue criterion such as Crossland for instance. Such an efficient approach can be found in [12] for instance**.** The aim of the present paper is only to compare the experimental residual stress fields analysed by X-ray diffraction [13,14] with those predicted from finite element modelling of the whole induction surface hardening process. Two specimen batches were prepared by varying the induction treatment parameters in order to obtain two different hardening depths. The residual stresses were analysed by X-ray diffraction in order to obtain the residual stress tensor at different depths from the surface to the core (below the hardened layer). Quasi-static compression tests were also carried out on both martensite and tempered martensite cylindrical specimens to assess their yield compressive strength. This property is a key parameter for the proposed multiphysic finite element modelling of the induction process.

2. Modelling of the induction heat treatment

2.1. Electromagnetic modelling

The electromagnetic and magneto-thermal parts of the induction surface hardening process have been modelled by using Flux 2D® software. This Finite Element Analysis (FEA) code is able to solve coupled magneto-thermal 2D axisymetric or plane

problems by considering the Maxwell's relationships ((I.1) to (I.4)) in a stationary state and two constitutive equations ((I.5) and (I.6)) for an homogeneous isotropic material [15]:

$$\mathrm{div}\vec{J} = 0 \tag{I.1}$$

$$\mathrm{div}\vec{B} = 0 \tag{I.2}$$

$$\overrightarrow{\mathrm{rot}}(\vec{E}) = -\frac{\partial \vec{B}}{\partial t} \tag{I.3}$$

$$\overrightarrow{\mathrm{rot}}(\vec{H}) = \vec{J} \tag{I.4}$$

$$\vec{B} = \mu_0 \mu_\mathrm{r}(H)\vec{H} \tag{I.5}$$

$$\vec{J} = \chi\vec{E} = \frac{\vec{E}}{\rho_\mathrm{e}} \tag{I.6}$$

Equations (I.1) and (I.2) express the conservative nature of the flux of both vectors $\vec{J}$ and $\vec{B}$ across a surface dS surrounding a volume dV of the heated workpiece. Equation (I.3) expresses that the time dependent magnetic field $\vec{B}$ inside the workpiece, induced by the alternative nature of the current inside the inductor, gives rise to an electric field inside the treated component, and thus the circulation of induced currents. As shown by equation (I.4), a current inside an electrical conductor, i.e., an electron displacement, generates a magnetic field around the conductor.

Solving equations (I.1)–(I.4) enables to determine $\vec{H}$, $\vec{B}$, $\vec{E}$ and $\vec{J}$ (Appendix A). The electromagnetic power density dissipated into the workpiece is then given by: $P_\mathrm{e} = (\vec{E}\cdot\vec{E})/\rho_\mathrm{e}$. This power density is integrated directly inside the heat relation (I.9) through $\dot{q}$. In order to solve a coupled magneto-thermal problem, the temperature dependence of the two constitutive equations is needed [17]:

$$B(H,T) = \frac{2J_\mathrm{s}}{\pi}(1 - \mathrm{e}^{(T-T_\mathrm{c}/C)})\mathrm{Arctg}\left(\frac{(a-1)\pi\mu_0 H}{2Js}\right) + \mu_0 H \tag{I.7}$$

$$\rho_\mathrm{e}(T) = \rho_0 + \rho_1 \mathrm{Artg}\left(\frac{T - T_\mathrm{c}}{T_\mathrm{r}}\right) \tag{I.8}$$

2.2. Thermal modelling

The temperature evolution inside a workpiece made of an homogeneous isotropic material is controlled by the well known heat equation expressed as follows:

$$\rho C_\mathrm{p}\frac{\mathrm{d}T}{\mathrm{d}t} - \mathrm{div}(\lambda\overrightarrow{\mathrm{grad}}(T)) = Q + \dot{q} \tag{I.9}$$

The power density related to the austenitic transformation during heating is not explicitly taken into account through the parameter $\dot{q}$ in equation (I.9), but through the specific heat temperature dependence [18,19] called equivalent specific heat. During cooling, the power density related to the martensitic transformation is neglected.

The thermal boundary condition applied over the free surface of the workpiece is:

$$\lambda\overrightarrow{\mathrm{grad}}(T)\cdot\vec{n} = -\varphi_\mathrm{c} \tag{I.10}$$

with:

$$\varphi_\mathrm{c} = h(T_\mathrm{s} - T_\mathrm{e}) \tag{I.11}$$

The heat loss by radiation is not taken into account in equation (I.10), being around two decades lower than the heat loss by convection at 1000 °C.

The thermal conductivity and equivalent specific heat temperature dependences are expressed as follow [15]:

$$\lambda = \lambda_0 + (\lambda_0 - \lambda_\infty)\exp\left(-\frac{T}{T_0}\right) \tag{I.12}$$

$$\rho C_\mathrm{p} = \frac{E_\mathrm{b}}{s_0\sqrt{2\pi}}\exp\left[\frac{-1}{2}\left(\frac{T - T_\mathrm{b}}{s_0}\right)^2\right] + (V_0 - V_\infty)\exp\left(\frac{-T}{T_1}\right) + V_\infty \tag{I.13}$$

The convection coefficient depends on the fluid in contact with the workpiece. During heating and initial air cooling before quenching, h is constant and equal to 50 W m^{-2} °C. During quenching, the fluid is highly convected water whose convection coefficient is expressed by the following relation [15]:

$$h = h_1 + h_2\exp\left(\frac{-(T - T_2)^2}{\tau_2}\right) + h_3\exp\left(\frac{-(T - T_3)^2}{\tau_3}\right) \tag{I.14}$$

2.3. Metallurgical modelling

The metallurgical modelling enables the calculation of the volume fraction of each metallurgical phase during the whole induction process, i.e. heating and subsequent quenching. The model is based on a principle of additivity in which an anisothermal transformation can be viewed as a succession of isothermal transformations [18–21]. The kinetics of an isothermal transformation is based on the Johnson–Mehl-Avrami law expressed as follow:

$$y = y_\mathrm{m}(T)(1 - \exp(-b(T)t_1^{\mathrm{c(T)}})) \tag{I.15}$$

The incubation time in anisothermal conditions is obtained when the Scheil coefficient, expressed as follow, equals unity [21]:

$$S = \int_0^\mathrm{t}\frac{\mathrm{d}t}{\tau(T)} = 1 \tag{I.16}$$

Equation (I.15) can be applied to the austenitic transformation during heating, the ferritic, pearlitic or bainitic transformations while cooling, as well as the tempering martensite tranformation.

The homogeneity of the austenite phase is known to depend on the austenitisation temperature T_a, and to modify its transformation during cooling. This phenomenon is taken into account

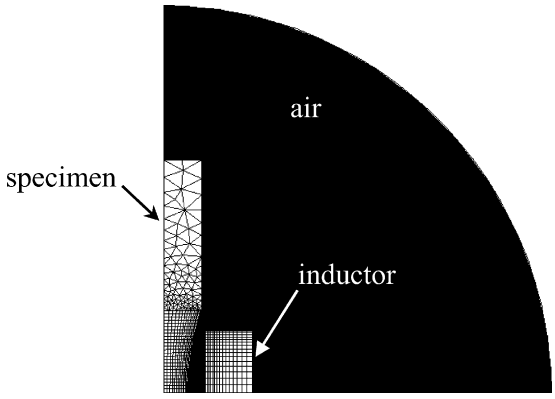

Fig. 1. Simulation configuration and mesh parts.

by introducing the b parameter depending on T_a in equation (I.15):

$$b(T, T_a) = (z - T)\alpha_b(T_a) \tag{I.17}$$

Heterogeneous austenite is obtained when $y = 1$ and $\alpha_b \neq 1$ in equation (I.15), while homogeneous austenite is achieved when both y and α_b reach unity. The specific characteristics of the martensitic transformation needs the previous relation to be modified as follow:

$$y = y_a(1 - \exp(-(M_s - T)^d)) \tag{I.18}$$

2.4. Mechanical modelling

The material is assumed to be homogeneous and isotropic. Each mechanical property p is deduced from a linear mixing law:

$$p = \sum_i y_i p_i \tag{I.19}$$

The material is assumed to obey to the Von-Mises plasticity criterion and its mechanical behaviour is modelled by an isotropic thermo-elastic perfectly plastic law with a flow stress σ_0. The total strain tensor ε_{ij} is considered as a sum of four tensors: (a) a thermal strain ε_{ij}^{th}, (b) an elastic strain ε_{ij}^{e}, (c) a plastic strain ε_{ij}^{p}, (d) a transformation strain ε_{ij}^{tr}. The latter is a sum of a strain resulting from the phase transformations and a strain related with the plasticity of transformation. This phenomenon is mainly influent for the martensitic transformation [22] and has been taken into account in our model through a decrease in the martensite yield stress. In the proposed methodology, the plastic strain due to martensitic transformation has not been physically modelled. Nevertheless, the effect of the plastic strain due to phase transformation is modelled by an indirect way which is practical and efficient for engineering applications. The martensite yield stress at room temperature is chosen in a reference database built as follow: cylindrical specimens are surface induction heat treated and the residual stress field is analysed (X-ray analysis). The martensite yield stress is then adjusted in order to get a good correlation between experimental and simulated residual stresses on the cylinder. The Young modulus at ambient temperature is the same for each metallurgical phase. The Young modulus is assumed to decrease linearly with temperature from 210 GPa at ambient temperature to 110 GPa at 1000 °C [15,27]. The poisson ratio is 0,3 for each phase. For each metallurgical phase, the flow stress is assumed to vary linearly with temperature from ambient temperature to 800 °C [15,28].

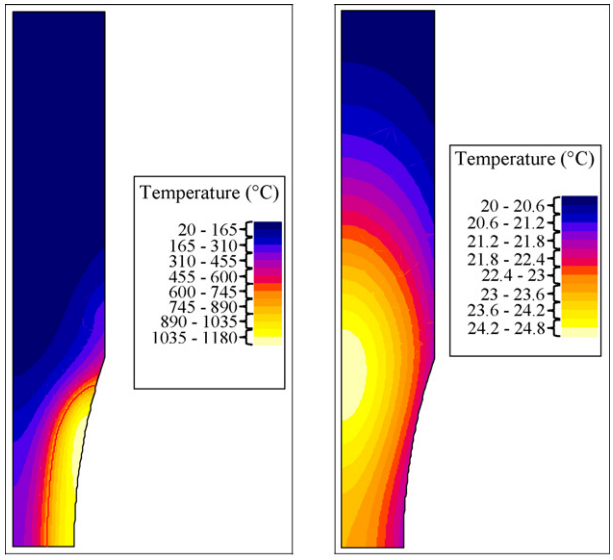

Fig. 2. Specimen thermal distribution (a) at the end of the induction heating process and (b) during quenching.

The coefficient of thermal expansion of each phase deduced from dilatometric tests is assumed constant with temperature [15].

2.5. Numerical modelling

The finite element software FLUX 2D®, able to solve coupled magneto-thermal problems, has been used to estimate the evolu-

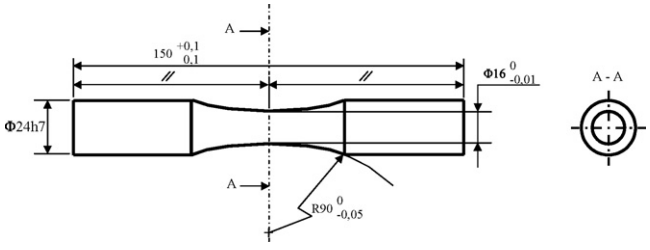

Fig. 3. Specimen geometry (dimensions in mm).

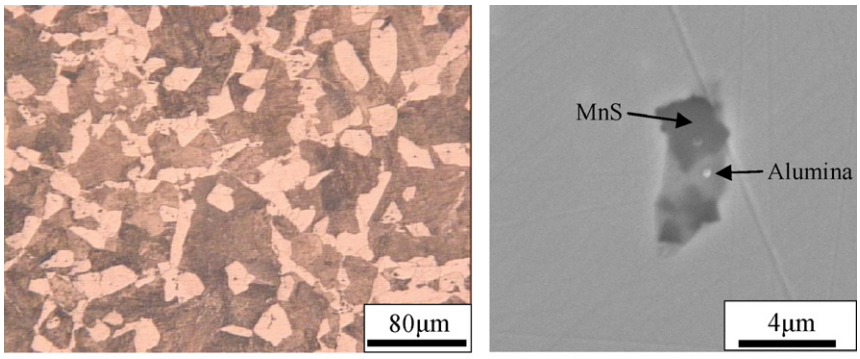

Fig. 4. (1) Microstructure of the studied untreated low alloyed carbon steel, (2) MnS inclusion surrounded by alumina.

Table 1
Chemical composition (wt%) and initial mechanical properties of the steel

C	Mn	Si	Al	S	V + Nb	Cr	Cu	Mo	Sn	E (GPa)	Rp0,2% (MPa)	Rm (MPa)
0.35	1.23	0.59	0.032	0.065	0.09	0.21	0.2	0.078	0.012	227	538	811

tion of the power density and temperature during the induction heating process. Fig. 1 describes the axisymmetrical configuration under study with the sample, inductor and air meshed regions.

After heating, FLUX 2D® is used to estimate the spatial and temporal evolution of the temperature during quenching. Fig. 2 shows an example of thermal distribution inside the specimen under study at the end of the induction heat ing process and during quenching.

The phase and hardness distribution inside the sample during quenching are calculated with the software METAL7® from the thermal patterns previously estimated with FLUX2D®. The thermal and phase distributions during quenching are then injected inside the finite element software MSC MARC® in order to estimate the residual stress fields.

3. Experimental procedure

3.1. Specimen geometry

Before surface induction hardening, smooth cylindrical specimens with a large median torus (Fig. 3) were machined for plane bending fatigue tests. Their theoretical stress concentration factor in bending is 1.02 [23]. The fatigue test results will be presented in a next paper since this item is devoted to the comparison between the experimental residual stresses and the simulated ones only.

3.2. Material and induction surface hardening treatment

Three batches of specimens are considered in this study: (a) untreated specimens with a normalised microstructure, (b) induction treated specimens with a hardening depth around 2 mm, (c) induction treated specimens with a hardening depth around 3 mm. The hardening depth is defined as the depth for which the Vickers hardness is 500HV10. Batches (b) and (c) are tempered at 180 °C during 1 h 30 min in an atmosphere controlled furnace after the induction treatment.

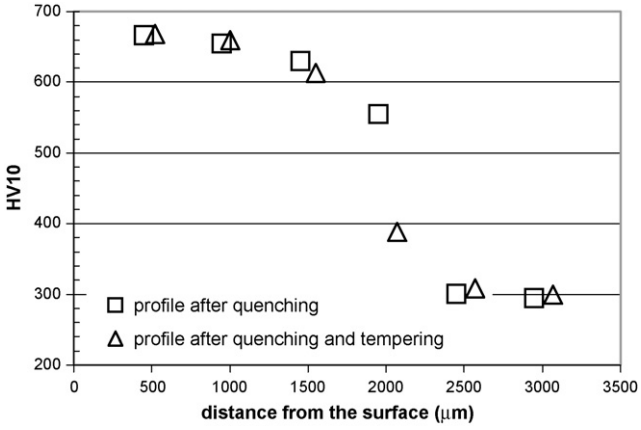

Fig. 5. Hardness profile for batch (b).

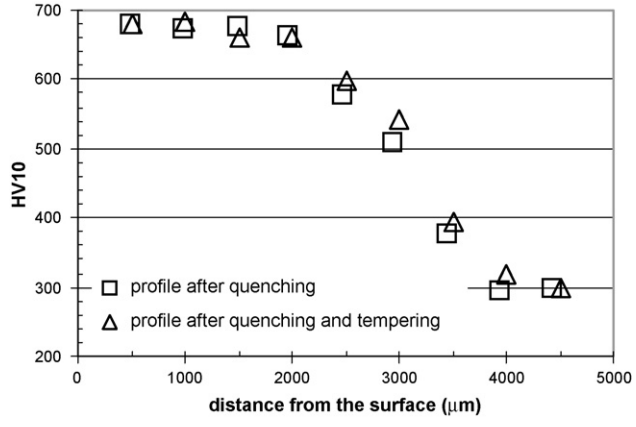

Fig. 6. Hardness profile for batch (c).

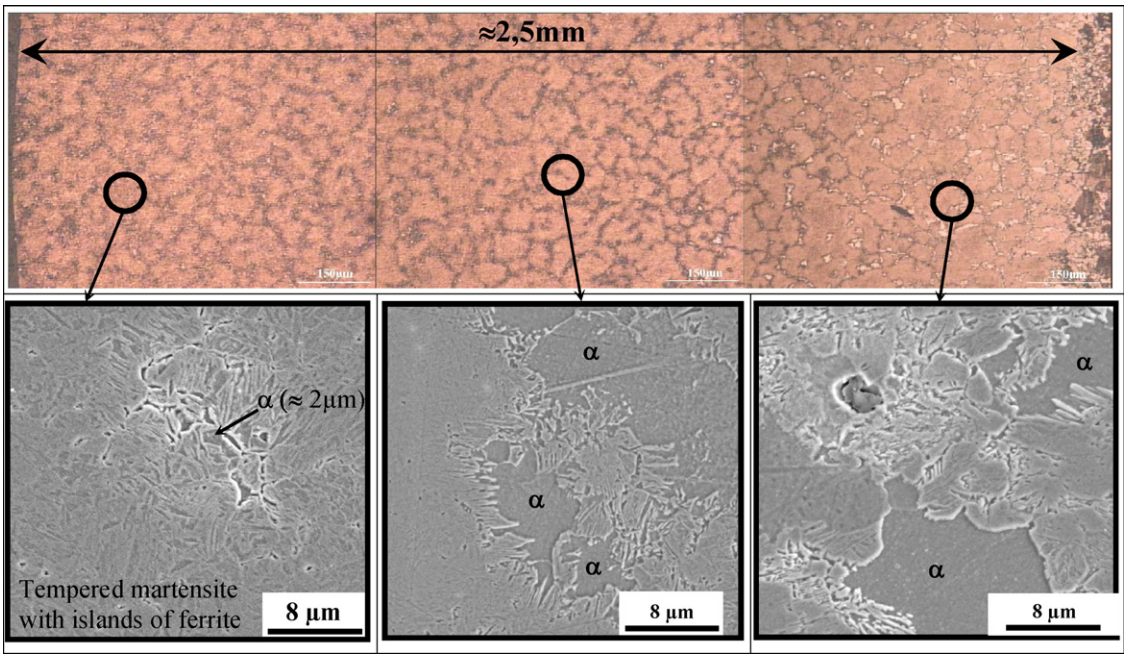

Fig. 7. Microstructures over the cross section of a specimen from the batch (b).Upper part: optical microstructures after nital etching; lower part: SEM pictures.

3.2.1. Induction hardening conditions

Specimens of the batches (b) and (c) were induction heat treated with a 20 kHz induction furnace and a one-turn coil whose inner diameter and length are respectively 27 mm and 40 mm. The heating power is 190 kW in both cases while the total heating time is 1.2 s and 1.6 s for batches (b) and (c) respectively. The time needed to reach the maximum power is 0.4 s. After heating, quenching is achieved with a delay of 0.5 s.

3.2.2. Material microstructures and Vickers hardness profiles

The investigated material is a low alloyed carbon whose chemical composition and initial mechanical properties are given in Table 1. The steel shows a normalised microstructure (Fig. 4.1) with a 300 HV Vickers hardness. MnS elliptic inclusions surrounded by a short alumina layer are present in this steel (Fig. 4.2). Their major axis is parallel to the longitudinal axis of the specimens. This is probably due to the cold rolling

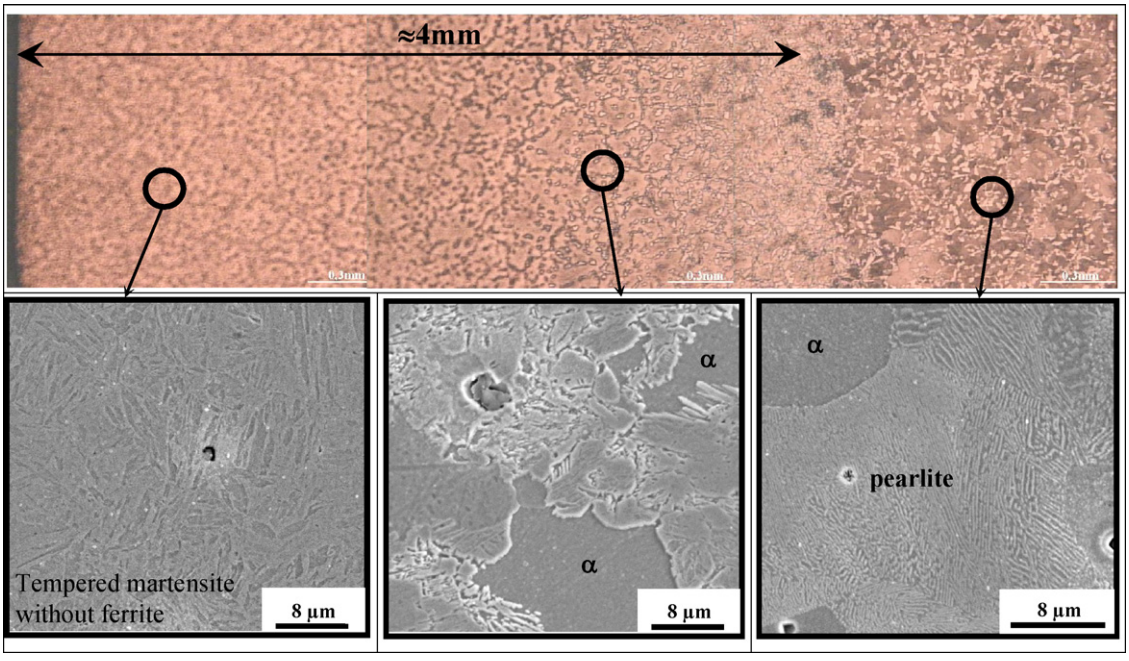

Fig. 8. Microstructures over the cross section of a specimen from the set (c). Upper part: optical microstructures after nital etching; lower part: SEM pictures.

process of the bars used to manufacture the specimens. Calcium is also found inside the inclusions. This element is usually added to give the inclusions a spherical shape.

From each hardened specimen batches, a specimen was cut in the smallest cross section of the median torus to measure the HV10 Vickers hardness profile (Figs. 5 and 6) and to examine the material microstructure (Figs. 7 and 8). The hardness profiles are shown for sets (b) and (c), respectively.

Examination of the microstructure along the cross section of a specimen from the batch (b) shows a mixture of martensite and ferrite from the surface until 2.5 mm in depth (Fig. 7). Near the surface, the volume fraction of ferrite is small, and it increases until 2.5 mm in depth. This justifies the hardness decrease from 680HV10 near the surface until 300HV10 at the transition area with the initial normalised microstructure. X-ray analysis indicates the absence of residual austenite inside the induction affected zone. Above 2.5 mm (in the core), the initial microstructure made of ferrite and pearlite is not affected by the induction heat treatment; its hardness is around 300HV10. The hardening depth is 2 mm according to the criterion defined earlier (500HV10).

Specimens of the batch (c) show a martensitic microstructure without ferrite from the surface until around 1 mm in depth with a hardness of 680HV10 (Fig. 8). Above 1 mm, the same microstructure as for the batch (b) can be observed. The transition area between the initial microstructure and the induction affected zone is now around 4 mm. The hardening depth is 3 mm according to the previous hardness criterion (500HV10).

According to Figs. 5 and 6, the hardness profiles before and after tempering are similar which means that the furnace tempering did not affect the properties of the martensitic hardened layer. It can be explained by considering that natural tempering occurs during quenching below the martensitic start temperature, M_S, as a result of a too small cooling rate. Thus, the tempering conditions during cooling (at low temperature) led to a stable metallurgical state with respect to those used in the furnace after quenching (180 °C–1 h 30 min). Residual stress profiles analysed before and after tempering were also similar which confirms the previous conclusion. Moreover, Fig. 9 shows

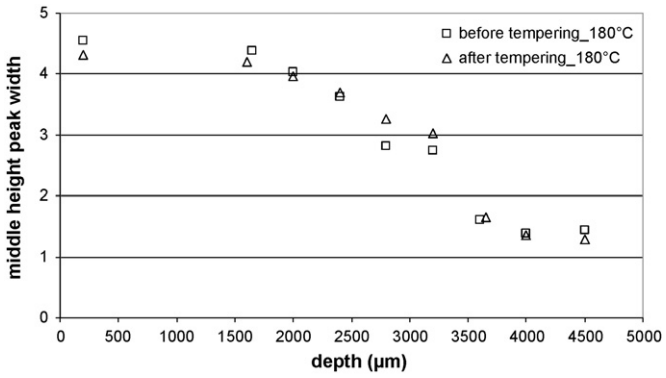

Fig. 9. Evolution of the middle height peak width within the depth of the material before and after artificial tempering.

the evolution of the middle height peak width within the depth of the material for two specimens of the batch (c): (i) after induction hardening and (ii) after induction hardening and tempering during 1 h 30 min at 180 °C. The width of the diffraction peak within the depth of the material is not significantly modified by the furnace artificial tempering. This means that there is no substantial hardening and microstructural modifications of the martensite layer during the furnace artificial tempering. This is in agreement with the hardness profiles and the assumption that natural tempering occurs during the induction heat treatment.

3.3. Martensite mechanical characterisation

Two batches of cylindrical specimens (tube) were machined from the same low-carbon steel. They were furnace heat treated to get either a martensitic or a tempered microstructure (180 °C – 1 h 30 min). The specimen geometry is a 21 mm long tube whose inner and outer diameters are 13 mm and 15 mm, respectively. These specimens were loaded in quasi-static compression to measure the yield stress and compressive strength of both microstructures.

The Vickers hardness of the quenched specimens is homogeneous over the cross section and around 50HV10 higher than that measured in the vicinity of the surface of induction hardened

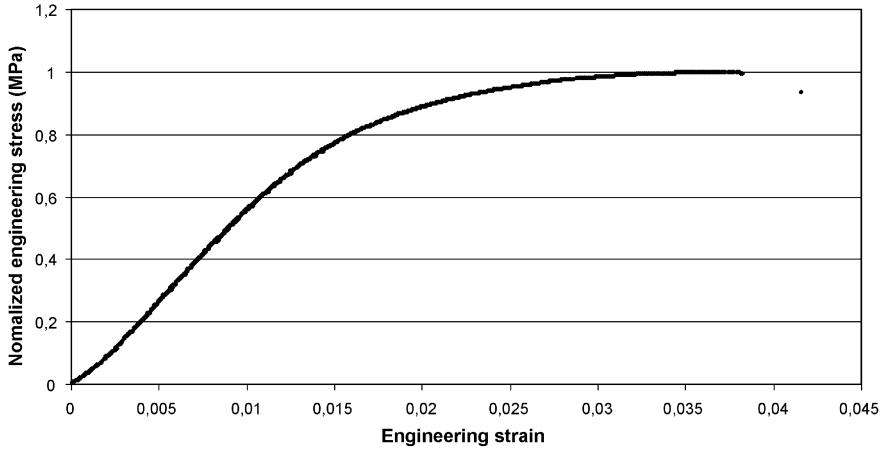

Fig. 10. Experimental normalized engineering stress versus engineering strain for a martensitic cylindrical specimen under compression.

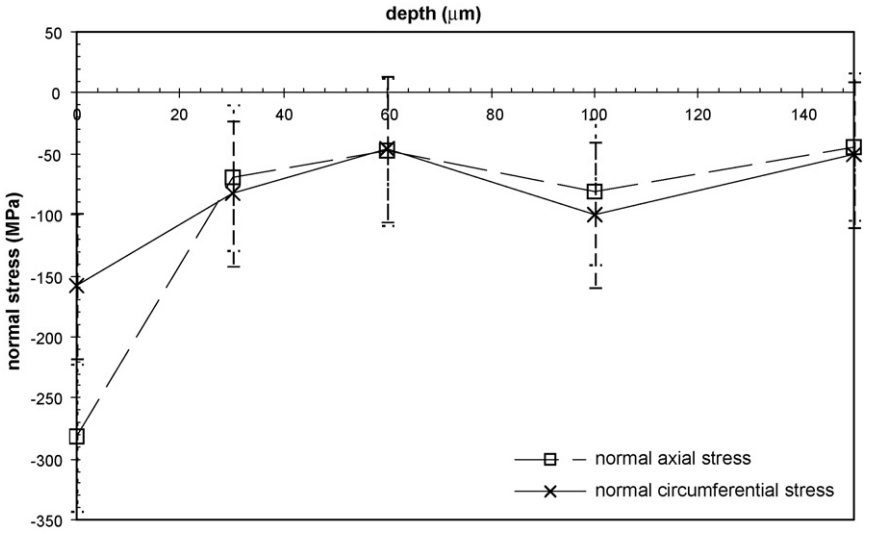

Fig. 11. Normal axial and circumferential residual stress profiles for two untreated specimens.

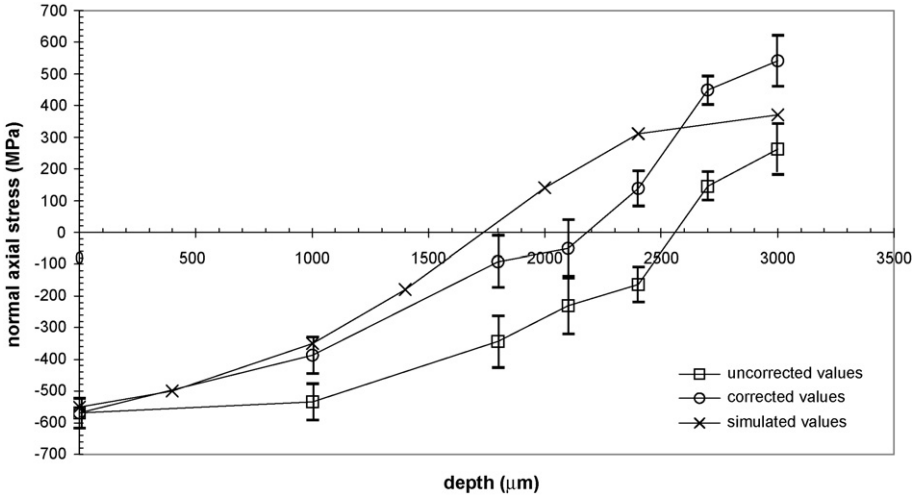

Fig. 12. Corrected, uncorrected and simulated normal axial residual stress profiles for an induction treated specimen with a hardening depth around 2 mm.

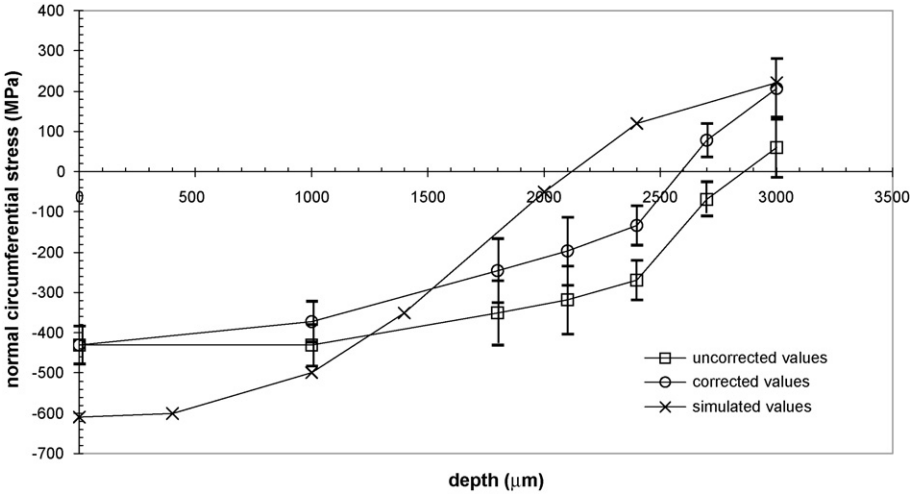

Fig. 13. Corrected, uncorrected and simulated normal circumferential residual stress profiles for an induction treated specimen with a hardening depth around 2 mm.

Table 2
Mechanical properties of martensitic cylindrical specimens in quasi-static compression

Heat treatment	Yield stress (MPa)	Maximum tensile strength (MPa)
Quenching	≈0.67	≈1
Tempering (180 °C)	≈0.5	≈0.71

specimens. After tempering, the hardness of the cylindrical specimens is similar to that measured on the fatigue specimens which confirms that natural tempering has occurred during quenching of those specimens. Quasi-static compression tests were carried out with a WOLPERT testing machine with a +/−200 kN load cell and a laser extensometer. A typical engineering stress/engineering strain curve for a martensitic specimen is shown in Fig. 10. The mechanical properties obtained for the two types of microstructures are shown in Table 2.

3.4. Experimental residual stress analysis conditions

Residual stress analysis was conducted by X-Ray Diffraction (XRD) according to the French standard AFNOR XP A 09–285 on may 1999 [13,14,15,16]. The classical "$\sin^2\psi$" method has been applied for stress evaluation with the use of 11 ψ angles (at least) for each stress value. A special compact stress analysis system SET-X was used with $\{2\,1\,1\}$ plane under $K_{\alpha 1}$ of Cr ($\lambda = 0.229$ nm). The following X-ray elastic constants were used: $1/2S_{2\{211\}} = 5.83 \times 10^{-6}$ MPa^{-1}, $S_{1\{211\}} = -1.28 \times 10^{-6}$ MPa^{-1}. The analysis zone is limited by a collimator of 1 mm in diameter. The obtained precision on stress analysis is better than 50 MPa which represents a deviation from linearity and comes from a Student's test of the used method considering an error risk of 35%. Because of the weak penetration depth of X-ray radiation on specimen (about 5 μm with 66% absorption of incident radiation), the measurements in sub-layer of specimens have been carried out after a local or circumferential electrolytic polishing. Material was removed at successive depths by controlling the removed depth. The process does not introduce any new stresses. The used electrolytical solution was a chlorine based acid electrolyte. The removed speed is about 1 μm/second under 50 V and 0.5 A/cm^2. The determination precision of removed depth is about 50 μm. Under local polishing, an adhesive mask is pasted on the sample to delimit an etching circle with a diameter about 8 mm. Two geometries of material removing techniques were used: local and circumferential electrochemical polishing (at the smallest cross section of the median torus of the specimens). Local material polishing is a fast technique compared to the circumferential material removing technique. It is known in literature [24,29] that the XRD results with the local polishing method can be considered as valid when the removal depth is lower than one-tenth the diameter for a cylindrical specimen. Beyond this value, the results should be corrected to account for the stress relaxation resulting from local material removal. According to the authors there is no reliable correction model available for this local removal technique. This means that the only possibility is to use the well-known Moore and Evans correction [24] developed for uniform material removal on a plane specimen. In this case the reliability of the corrected results is doubtful. Circumferential polishing is a quite slow technique, for which a correction model is also needed. In that case, the Moore and Evans model is known to overestimate the correction, which means that the true residual stresses must be considered between the uncorrected and cor-

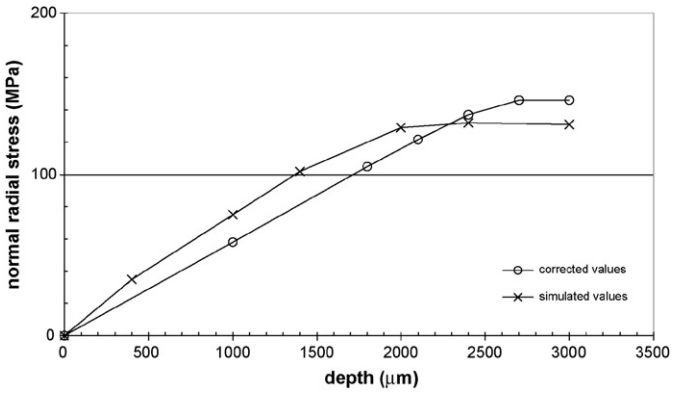

Fig. 14. comparison between the simulated and Moore/Evans estimated normal radial residual stress profiles.

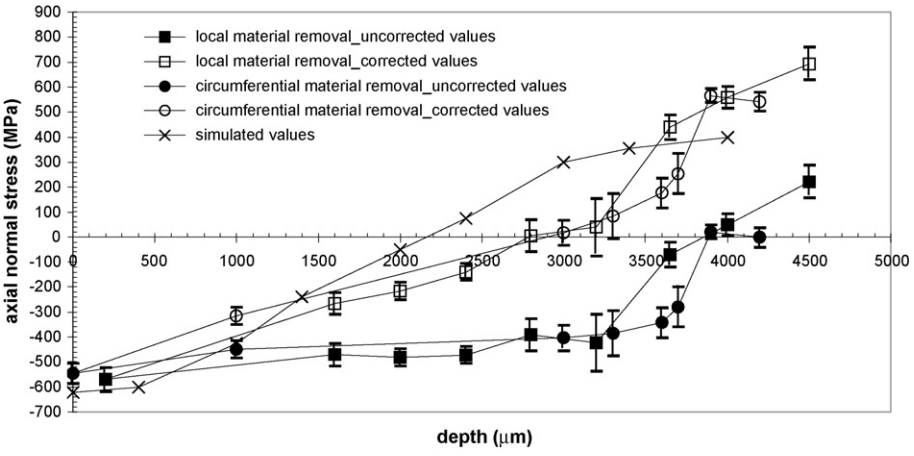

Fig. 15. Corrected, uncorrected and simulated axial normal residual stress profiles for both material removal techniques for case c (3 mm).

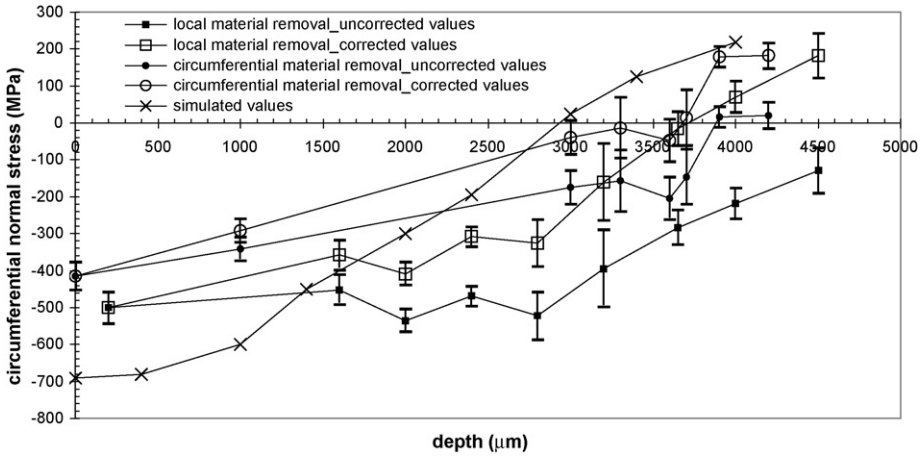

Fig. 16. Corrected, uncorrected and simulated circumferential normal residual stress profiles for both material removal techniques.

rected results, especially until one tenth the specimen diameter. At higher depth, the reliability of the correction is not really known. An interesting aspect of the Moore and Evans correction model is to give an estimation of the normal radial stress which cannot be directly deduced from experimental analysis. The existence of this normal radial stress below the heat treated specimen surface is undoubtful with a mechanical point of view, and this is very important for a good estimation of the hydrostatic stress, which is of prior importance in the fatigue crack initiation. The hydrostatic stress is a key parameter in multiaxial fatigue strength assessment methods such as proposed by Crossland [10], Papadopoulos [25] or Morel [26] for instances. In the case of our paper, the multiaxiality of residual stresses has to be considered even if the loading creates a uniaxial stress state only (bending). An example of the application of a multiaxial fatigue criterion to surface induction hardening is given in Dumas et al. [12] and will be detailed in a next paper.

4. Comparison between residual stress analysis and simulation, discussion

In the following, residual stresses are always indicated in cylindrical coordinates where σ_{rr}, σ_{zz} and $\sigma_{\theta\theta}$ are respectively the radial, axial and circumferential normal stresses.

4.1. Untreated specimens (batch a)

Fig. 11 illustrates the normal axial and circumferential residual stress profiles for an untreated fatigue specimen. Residual stress analysis is made after local electrochemical polishing because of the presumed localisation of residual stresses close to the specimen surface. The results shown in Fig. 11 are not corrected with the Moore and Evans proposal.

The machining induced residual stresses are mainly localized in the vicinity of the specimen surface until around 60 μm. In this area, the residual stresses σ_{zz} and $\sigma_{\theta\theta}$ are compressive with a quite small maximum value at the specimen surface.

4.2. Induction treated specimens with a hardening depth around 2 mm (batch b)

Figs. 12–14 show the axial, circumferential and radial normal residual stress profiles for an induction treated specimen with a hardening depth around 2 mm. X-ray analysis was conducted after local electrochemical polishing and the results are

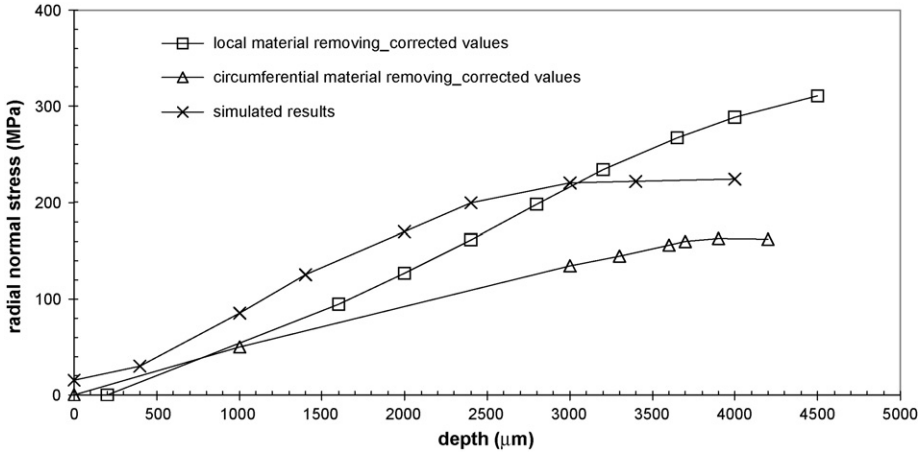

Fig. 17. comparison between the simulated and Moore/Evans estimated radial normal residual stress profiles for both material removal techniques.

presented either with or without Moore and Evans correction. The simulated results are also shown in Figs. 12–14.

As shown in Figs. 12 and 13, for both normal stresses σ_{zz} and $\sigma_{\theta\theta}$, the residual stress field is compressive over the two first millimetres and then in tension. The maximum compressive stress is quite small in surface which might result from natural tempering occurring during quenching below M_S. The Moore and Evans correction gives rise to a tensile normal radial stress with a maximum value around 150 MPa (Fig. 14). Considering the normal radial stress, the experimental (corrected value) and simulated results are in very good agreement (Fig. 14). Taking into account the experimental uncertainties, the best agreement between experiments and σ_{zz}, $\sigma_{\theta\theta}$ simulated results is obtained when applying the Moore and Evans correction after local polishing. In that case, simulated and experimental results are in fairly good agreement until around one tenth the specimen diameter, i.e. 1.6 mm. In the vicinity of the transition between the initial and quenched microstructures, the maximum mismatch is around 300 MPa.

4.3. Induction treated specimens with a hardening depth around 3 mm (batch c)

Figs. 15–17 illustrate the normal axial, circumferential and radial residual stress profiles for an induction treated specimen with a hardening depth around 3 mm. X-ray diffraction analysis was conducted after two types of material removal techniques: local or circumferential electrochemical polishing. The results are presented either with or without Moore and Evans correction. The simulated results are also shown in Figs. 15–17.

Comparison between the simulated results and those obtained after local polishing exhibits a greater mismatch. The mismatch cannot be attributed to the mesh quality as any refinement did not enable to improve the results. The mismatch should be explained by a not enough precise material modelling in terms of material properties and their evolution with temperature. In that way, the linear mixture law used to assess various properties of multiphasic microstructures encountered during the whole heat treatment process should be considered as doubtful, for example, in the case of a mixture of soft ductile austenite and hard martensite. Also, the finite element model does not take into account, as a boundary condition, the fact that a low axial force is applied to the specimen during the induction process. This should give rise to some local plasticity around the smallest cross section of the specimen at high temperature during austenitisation with a resulting modification of the stress field both at high temperature and then later after quenching. Finally, one can point out the actual unknown validity of X-ray diffraction results (experimental data and correction method) at such large depth (quite larger than one tenth the specimen diameter).

4.4. Effect of the material removal technique on the residual stresses analysed by X-ray diffraction

Due to the large depth analysed for the heat treated specimens (especially in the case c, i.e. 3 mm) the validity of the local polishing technique (even with the Moore and Evans correction) is not demonstrated. To clarify this important point a set of XRD analysis was carried out on specimens with the circumferential polishing technique. Residual stresses analysed by both the local polishing and the circumferential polishing are compared in Figs. 15–17 with or without the Moore and Evans correction.

The corrected axial normal stress profiles after local or circumferential polishing (Fig. 15) are quite close even at high depths and in fairly good agreement with the simulated profile. The corrected circumferential normal stress profiles after local or circumferential polishing (Fig. 16) are not so close as in Fig. 15 and it is quite difficult to conclude about the more suitable polishing technique. At low depths below one tenth the sample diameter, the corrected results after local polishing are closer to the simulated results, while at deeper depths, the corrected stress profile resulting from a circumferential polishing correlates much better the simulated results. Concerning the radial normal stress profile, the corrected results after local polishing are fairly close to the simulated results except at large depths higher than 4000 μm, while the corrected stress profile resulting from a circumferential polishing is underestimated with respect to the simulated profile. From these comments, there is no clear evidence about the best suitable polishing technique. At low depths, the local polishing technique should be preferred while at deeper depths, the choice is not so clear. Considering that circumferential polishing is a slow technique, the authors would rather recommend the use of the local polishing technique.

5. Conclusion

The induction hardened specimens may suffer natural tempering during quenching below the martensitic start temperature. This phenomenon leads to a maximum hardness in the surface of the specimens lower than it should have been observed after pure quenching. It also affects the maximum compressive residual stress value in the hardened layer. Finite element modelling of the whole induction process shows very good residual stresses predictions when compared with those measured by X-ray analysis, especially for depth lower than one tenth the specimen diameter. Above this value, the maximum mismatch between the simulated and experimental results of the axial normal stress σ_{zz}, and the circumferential normal stress $\sigma_{\theta\theta}$ reaches around 300 MPa. This should be due to two main reasons. On one hand, the reliability of the experimental technique for deep analysis by X-ray diffraction is doubtful. On the other hand, this difference between simulation and experiments can be due to the following reasons: (i) the lack of precision in the description of the material properties evolution with temperature, (ii) the presumed unreliability of the linear mixture law used for some multiphasic material properties estimations in simulation and (iii) the plasticity due to the metallurgical transformation is neglected.

Concerning the X-ray diffraction drawback, the authors imagine that for surface induced hardened specimens, it should be interesting to use a non destructive technique so that Neutron diffraction to investigate residual stress field at large depth. Nevertheless, due to the large volume analysed (compared with the one analysed by XRD) such non destructive technique might also be difficult to use for estimating stress gradient. But, for the

lack of precision in the finite element modelling of the whole induction process, discussion about the most influent contribution to the observed mismatch is actually very difficult to propose.

Appendix A

Solving relations (I.1) to (I.4) can be performed by considering two potentials: a vector $\vec{A}$ and a scalar V so that:

$$\vec{B} = \overrightarrow{\text{rot}}(\vec{A}) \tag{A.1}$$

$$\vec{E} = -\frac{\partial \vec{A}}{\partial t} - \overrightarrow{\text{grad}}(V) \tag{A.2}$$

Equations (A.1) and (A.2) leads to the following relation for the conducting regions:

$$\overrightarrow{\text{rot}}\left(\frac{\overrightarrow{\text{rot}}(\vec{A})}{\mu(\vec{H})}\right) + \sigma\frac{\partial \vec{A}}{\partial t} = -\sigma\overrightarrow{\text{grad}}(V) \tag{A.3}$$

In the insulated regions, equation (A.3) can be simplified as follow:

$$\overrightarrow{\text{rot}}\left(\frac{\overrightarrow{\text{rot}}(\vec{A})}{\mu(\vec{H})}\right) = \vec{0} \tag{A.4}$$

The boundary conditions are either Dirichlet or Neumann-type along a given surface depending whether $\vec{B}\cdot\vec{n} = 0$ or $\vec{B}\wedge\vec{n} = 0$ has to be satisfied. Continuity conditions between regions of different properties are also added as follow:

$$(\vec{H}_2 - \vec{H}_1)\wedge\vec{n} = \vec{0} \tag{A.5}$$

$$(\vec{E}_2 - \vec{E}_1)\wedge\vec{n} = \vec{0} \tag{A.6}$$

$$(\vec{B}_2 - \vec{B}_1)\cdot\vec{n} = 0 \tag{A.7}$$

$$(\vec{J}_2 - \vec{J}_1)\cdot\vec{n} = 0 \tag{A.8}$$

References

[1] H. Kristoffersen, P. Vomacka, Mater. Des 22 (2001) 637–644.
[2] J. Grum, Mater. Sci. For. 347–349 (2000) 453–458.
[3] L. Bertini, V. Fontanari, Int.J. Fatigue 21 (1999) 611–617.
[4] M. Melander, J. Heat Treating 4 (1985) 145–165.
[5] X. Dong-Hui, K. Zhen-Bang, J. Eng. Mater. Technol. 118 (1996) 571–575.
[6] X. Kewei, H. Naisai, Z. Huijiu, Eng. Fract. Mech. 54 (2) (1996) 171–176.
[7] D.H. Breen, E.M. Wene, Fatigue in Machine Structures (ground vehicles), Fatigue and Microstructures, ASM, Metals Park (OH), 1979, p.88.
[8] X. Kewei, H. Jiaven, Z. Huijiu, Int. J. Fatigue 16 (5) (1994) 337–343.
[9] A. Tjernberg, Eng. Fail. Anal. 9 (2002) 45–61.
[10] B. Crossland, Int. Conf. Fatigue Met., IME/ASME, London, 1956.
[11] N. Skally, J.F. Flavenot, CETIM Inform. 90 (1985) 35–47.
[12] C. Dumas, T. Palin-Luc, D. Coupard, P Bristiel, V Ji, Proceedings of the Metal 2007, Hardec nad Moravici, Czech Republic, 2007, ISBN 978-80-86840-33-8.
[13] P.S. Prevey, X-ray diffraction residual stress techniques, in: Metal Handbook, vol. 10, ASM International, Materials Park, OH, 1986.
[14] P.C. Prevey, P.W. Mason, in: C. Ruud (Ed.), The Use of X-ray Diffraction to Determine the Triaxial Stress State in Cylindrical Specimens, (Practical applications of residual stress technology), ASM, 1991.
[15] Bristiel P., Modélisation magnétothermique, métallurgique et mécanique de la trempe superficielle après chauffage par induction appliquée aux vilebrequins, PhD thesis, ENSAM CER de Bordeaux, (2001), France.
[16] Méthodes d'essais pour l'analyse des contraintes résiduelles par diffraction des rayons X," XP A 09-285, AFNOR Normalisation Française, (May 1999).
[17] Garron de la Morinais G., Meunier G., Kieny C., Calcul des courants de Foucault en trois dimensions par une formulation utilisant le potentiel vecteur magnétique et le potentiel scalaire électrique, Revue Physique Aplliquée, (1990), pp. 593–603.
[18] Durban C., Analyse et optimisation des paramètres influents sur le calcul prévisionnel des contraintes résiduelles conséquentes au chauffage superficiel par induction suivi d'une trempe, PhD thesis, ENSAM CER de Bordeaux, (1997), France.
[19] Barrere E., Contribution à la modélisation des contraintes résiduelles lors de la trempe superficielle au défilé après un chauffage par induction, PhD thesis, ENSAM CER de Bordeaux, (1992).
[20] M. Gergely, S. Somogyi, G. Buza, Conference Calculation of Internal Stresses in Heat Treatment of Metallic Materials, Linköping (Suède), 1984.
[21] J.B. Leblond, G. Mottet, J. Devaux, Mater. Sci. Technol. 1 (1985) 815–822.
[22] S. Denis, D. Farias, A. Simon, ISIJ Int. 32 (1992) 316–325.
[23] R.E. Peterson, Stress Concentration Factors, Wiley-Interscience Publication, 1974.
[24] M.G. Moore, W.P. Evans, SAE Trans. 66 (1958) 340–345.
[25] I.V. Papadopoulos, Int. J. Fatigue 16 (6) (1994) 377–384.
[26] F. Morel, Fatigue Fract. Mater. Struct. 21 (3) (1998) 241–256.
[27] Propriétés des aciers 35M5, Dossier technique OTUA, 1980.
[28] A. Bokota, S. Iskierka, Int. J. Mech. Sci. 40 (6, June) (1998) 617–629.
[29] M. Belassel, Etude de la distribution des contraintes d'ordre I et II par DRX dans un acier perlitique, PhD Thesis, n(ENSAM 1994-01, (1994), France.